Dynamics of femtosecond laser ablation studied with time-resolved x-ray absorption fine structure imaging

Katsuya Oguri,* Yasuaki Okano,† Tadashi Nishikawa, and Hidetoshi Nakano
NTT Basic Research Laboratories, Nippon Telegraph and Telephone Corporation, 3-1 Morinosato Wakamiya, Atsugi, Kanagawa 243-0198, Japan

(Received 17 September 2008; revised manuscript received 17 November 2008; published 3 April 2009)

We studied the dynamics of the femtosecond laser ablation of aluminum in an energy range well above the ablation threshold with the ultrafast time-resolved x-ray-absorption fine structure imaging technique. Analyzing the spectral structures near the *L* absorption edge that appeared in one-dimensional images of soft-x-ray absorbance, we successfully identified doubly and singly charged ions, neutral atoms, liquid nanoparticles, and possible atomic clusters in the expanding ablation plume. We also clarified that the ejected particles depend strongly on the laser irradiation intensity. The spatiotemporal evolution of the ablation particles allows us to estimate the spatial distribution of atomic density and the ejection velocity of each type of particle. In particular, we discuss the temporal sequence of the particle ejection in the early stages of plume expansion. Our experimental results strongly support the idea that photomechanical fragmentation and vaporization are dominant mechanisms for the production of liquid nanoparticles and neutral atoms, respectively, in femtosecond laser ablation induced in an irradiation intensity range of 10^{14}–10^{15} W/cm^2.

DOI: 10.1103/PhysRevB.79.144106 PACS number(s): 79.20.Ds, 52.38.Mf, 61.05.cj

I. INTRODUCTION

Femtosecond laser ablation is attracting a lot of attention as a unique material processing technique that provides distinct advantages in certain applications over the use of nanosecond laser ablation. The applications cover a wide range of technology including precise micromachining (Refs. 1 and 2, and references therein), unique material synthesis,[3,4] thin-film growth with fine and high quality particles,[5,6] and nanosurgery related to cells and tissue.[7] These attractive applications have stimulated interest in a physical understanding of the mechanisms of femtosecond laser ablation, particularly in its early stages, in order to control the ablation process and realize a highly advanced processing technique. The comprehensive dynamics that lead to ablation after femtosecond laser irradiation are currently being studied theoretically using molecular dynamics or hydrodynamics.[8–16] This is because there are still considerable difficulties involved in identifying ablation particles experimentally and measuring their physical properties such as temperature, pressure, velocity, and density, which evolve on a picosecond to subnanosecond temporal scale and submicrometer to micrometer spatial scale. Thus, experimental approaches for clarifying the physical mechanisms of femtosecond laser ablation are very limited.

In spite of these experimental difficulties, some mechanisms have been proposed based on experimental interpretations. One such mechanism is the complete vaporization of ejected material without employing a melting process as described by Chichkov and co-workers.[17–19] This was proposed based on their microscopic observations of an ablated hole on a metal sample after femtosecond laser irradiation. The sharp and well-defined shapes without a trace of molten material that are typically observed for nanosecond and picosecond laser ablated holes led to the conclusion that the main mechanism during the ablation process is a direct transformation from the solid phase to the vapor or the plasma phase. Although this conclusion was simple and rough, the experimental findings triggered research on the precise micromachining of materials with femtosecond laser ablation. Another mechanism was subsequently proposed by Sokolowski-Tinten and co-workers[20–22] based on ultrafast time-resolved microscopy observations. They observed a transient optical interference fringe with a nanosecond scale duration in the ablated area on the surface of metal and semiconductor samples. They interpreted this to mean that the interference fringe appears as a result of the production of an inhomogeneous mixed phase of gas and liquid particles. They proposed that this mixture of gas and liquid particles is produced via the nucleation of gas bubbles, which is often referred to as a phase explosion mechanism.[23] Regrettably, their method was unable to identify the mixture of gas and liquid particles directly despite its subpicosecond temporal resolution because it only obtained information about the change in the optical reflectivity of the ablated material. Recently, the synthesis of nanometer-sized particles via femtosecond laser ablation was confirmed by atomic force microscopy.[6,24,25] It was also supported by the observation of a characteristic structureless emission spectrum from the nanoparticles with time-gated optical emission spectroscopy (OES).[6,16] In these studies, the nanoparticle production mechanism was also interpreted as a phase explosion based on the discussions found in the Sokolowski-Tinten studies.[16,25] However, the time-gated OES is unsuitable for investigating ablation dynamics due to its microsecond temporal resolution, which is insufficient for measuring the early stages of the ablation process.

These experimental observations and interpretations are supported by theoretical studies using the molecular-dynamics method. By calculating the thermodynamic trajectories of the system after the femtosecond laser energy deposition, they showed that the dominant mechanism of femtosecond laser ablation is vaporization when the laser fluence is sufficiently high and phase explosion when it is

near the ablation threshold.[10–16] Moreover, recent studies by Perez and Lewis[10–12] predicted the possibility of a different mechanism, which they call photomechanical fragmentation, when the laser fluence is above the ablation threshold but below the minimum fluence of vaporization. In addition, spallation and trivial fragmentation have also been proposed as femtosecond laser ablation mechanisms. Thus, we are gradually reaching a detailed understanding of the femtosecond laser ablation mechanism as a result of the combination of experimental and theoretical studies.

With a view to investigating the ultrafast dynamics of the femtosecond laser ablation process and its physical mechanism experimentally, we have developed an imaging system for ultrafast time-resolved soft-x-ray absorption spectroscopy (XAS) (Ref. 26) by developing the pioneering idea of using a laser-produced plasma source to observe an ablation plume.[27,28] This is because XAS, particularly x-ray absorption fine structure (XAFS) spectroscopy, is known to be sensitive to the local electronic state that provides information about chemical bonding or the local structure of a material. This suggests that our system has great potential to develop into one of the most suitable tools for investigating the laser ablation process, where ablated materials change instantaneously and evolve spatiotemporally. In our system, the idea of combining an ultrashort soft-x-ray pulse source emitted from femtosecond-laser-produced plasma and an imaging apparatus based on a Kirkpatrick-Baez (KB) (Ref. 29) microscope has enabled us to measure successfully spatially resolved soft-x-ray absorption spectra in the 50–150 eV energy range of a femtosecond laser ablation plume of aluminum.[30] Recently, we considerably improved the spectral resolution of this system to achieve XAFS measurements and we employed the system to measure the expansion of a femtosecond laser ablation plume. As a result of this improvement, we successfully identified the nanoparticle component of the plume by analyzing a fine structure near the aluminum L absorption edge.[31]

In this paper, we report our study of the dynamics of the femtosecond laser ablation of aluminum induced in an irradiation intensity range of 10^{14}–10^{15} W/cm^2 with our ultrafast XAFS imaging system. We clearly identify different ejected particles in the ablation plume based on the spectral structures near the L absorption edge of aluminum and estimate the atomic density and ejection velocity of each type of ablation particle. We use these results as a basis for discussing the femtosecond laser ablation mechanism in an energy range extending from well above the ablation threshold to near the plasma formation.

II. EXPERIMENT

A. Ultrafast XAFS imaging system

Figure 1 is a schematic illustration of the ultrafast time-resolved XAFS imaging system. This system takes its basic design from the imaging system for time-resolved soft-x-ray absorption spectroscopy that we developed previously.[26,30] Here, we provide a detailed description of our ultrafast time-resolved XAFS imaging system that we briefly mentioned in a recent study.[31] The most characteristic feature of the system is the combination of a femtosecond-laser-pump and picosecond-soft-x-ray-probe arrangement and a soft-x-ray absorption imaging arrangement. The system employs a chirped pulse amplification system consisting of a Ti:sapphire laser with a central wavelength of 790 nm, a pulse width of 100 fs, a repetition rate of 10 Hz, and an extinction ratio between the main pulse and the undesirable satellite pulse of better than 10^6. The output laser pulse with an energy of 50 mJ was divided into two pulses: one to generate soft x rays and the other to produce an ablation plume. The former passed through an interferometer to produce a pulse pair, while the latter passed through an optical delay line to adjust the relative time between the production of the plume and the soft-x-ray probe. The soft-x-ray pulse was generated from femtosecond-laser-produced plasma that was induced by focusing the pulse pair onto a tantalum tape target with a thickness of 25 μm. The soft-x-ray pulse from the tantalum plasma has a broadband continuum spectrum without any intense emission line in the soft-x-ray region and so is suitable for absorption spectroscopy. The emitted soft-x-ray pulse was directed into the ablation plume by a Ni-coated ellipsoidal condenser mirror. The beam diameter of the soft-x-ray pulse was about 400 μm in the interaction region. The laser ablation plume was produced by focusing the other laser pulse onto a 40 μm thick aluminum tape sample, which was scanned to refresh the tape surface at each laser shot. The peak intensity of the focusing laser pulse ranged from 1.8×10^{14} to 8.5×10^{14} W/cm^2. When we consider the extinction ratio of the laser pulse, the laser ablation was probably induced by a direct laser-solid interaction without any influence from preformed plasma. The produced ablation plume expands dominantly into a vacuum in a direction perpendicular to the tape surface. The soft-x-ray pulse probes the plume at a right angle to the plume expansion direction. We positioned the tape surface near the center of the soft-x-ray beam to probe the plume with an intense region of the beam. With this positioning, we were able to measure the plume expansion about 300 μm from the tape surface. A soft-x-ray backlit image of the ablation plume was transferred to a soft-x-ray detector with a KB microscope at a magnification of about 10. By placing a transmission grating with a 50 μm slit whose opening parallels the plume expan-

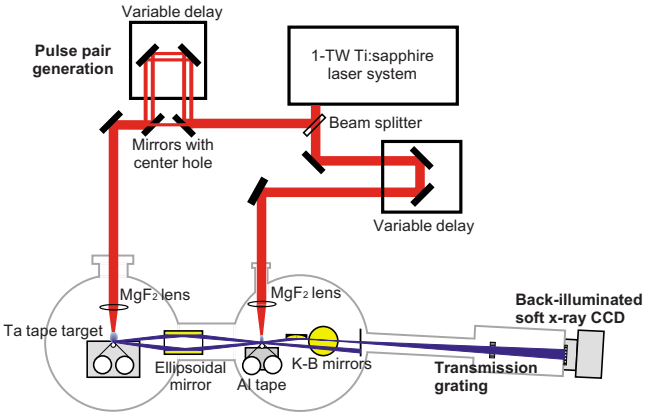

FIG. 1. (Color online) Schematic illustration of the ultrafast time-resolved XAFS imaging system.

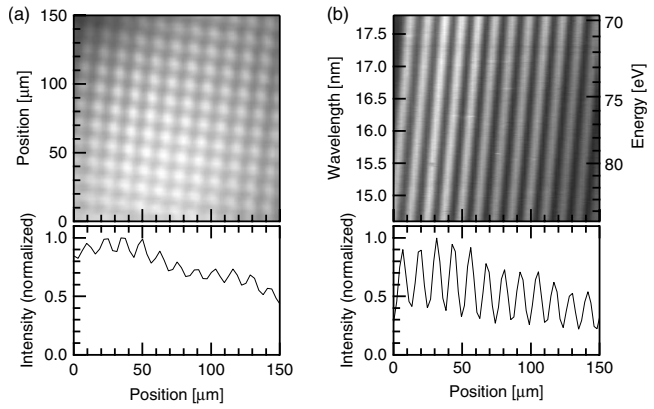

FIG. 2. (a) Typical soft-x-ray backlit image and its cross section of a copper mesh constructed of 5 μm bars with a 12.5 μm period and (b) a spectrally resolved soft-x-ray backlit image and its profile at 16 nm of the same mesh.

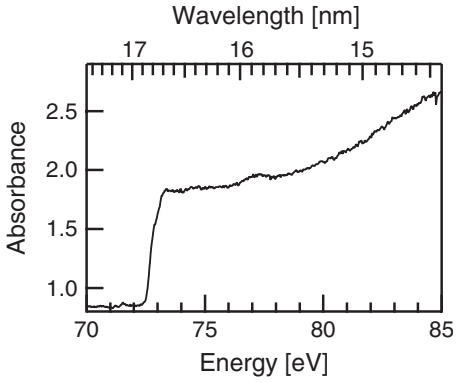

FIG. 3. Absorbance spectrum of 100 nm thick aluminum thin film. The sharp edge structure at 72 eV corresponds to the $L_{II,III}$ absorption edge of solid aluminum.

sion direction before the detector we were able to obtain soft-x-ray absorption spectra of the plume with its one-dimensional spatial distribution in the plume expansion direction. To realize XAFS measurements, we improved the spectral resolution compared to that of our previous system[26,30] by using a high-resolution transmission grating with a line spacing of 10 000 grooves/mm and a back-illuminated x-ray charge-coupled device (CCD) detector with 25 μm pixels. The deterioration of the soft-x-ray signal that resulted from using this high-resolution transmission grating was compensated for by the soft-x-ray enhancement effect realized with a double pulse excitation scheme.[32,33] We generated a pulse pair with a separation time of 3 ns using the interferometer that consisted of center-holed mirrors rather than beam splitters. The peak intensities of the prepulse and the main pulse were 9×10^{14} and 2×10^{16} W/cm^2, respectively. Since the excitation condition is very similar to that previously reported,[26,30] we estimated the pulse duration of the emitted soft x ray to be about 30 ps, which corresponds to the temporal resolution of the system. Although the double pulse excitation scheme is known to increase the pulse duration of the laser-produced-plasma soft x ray more than the single pulse excitation scheme,[33] the 30 ps duration is sufficiently short for the plume expansion dynamics to be measured.

B. Estimation of spatial and spectral resolution

To test to the spatial resolution of the system, we measured a soft-x-ray backlit image and its cross section. The image was of a copper mesh constructed of 5 μm bars with a 12.5 μm period (Fig. 2). As seen in Fig. 2(a), the grid pattern of the mesh is resolved but the contrast of the image is not very high. This can be explained by the diffraction effect caused by a relatively intense component with longer wavelengths that comprises a tantalum plasma emission. With a spectrally resolved backlit image of the mesh [Fig. 2(b)], the contrast is significantly improved because the measured soft-x-ray component is limited to the 70–85 eV (14.5–17.5 nm) region. This result confirms that the spatial resolution of the system is approximately 12.5 μm in this energy range. We also measured the $L_{II,III}$ absorption edge of solid aluminum using an aluminum thin film with a thickness of 100 nm as a sample in order to estimate the spectral resolution of the system (Fig. 3). This figure clearly shows a sharp increase in soft-x-ray absorption that corresponds to the $L_{II,III}$ absorption edge of solid aluminum. In addition, there is a bend in the edge slope, thus indicating that the system can resolve the spin-orbit splitting of the absorption edge, i.e., the L_{II} and the L_{III} edges. Since the energies of the L_{II} and the L_{III} edges correspond to 73.15 and 72.71 eV, respectively,[34] the resolving power of the system, $E/\Delta E$, is estimated to be about 180 with a spectral resolution ΔE of 0.44 eV, which is much better than that of our previous system.[26,30] Thus, the improvement in the spectral resolution enabled us to measure fine structures near the $L_{II,III}$ absorption edge of aluminum.

III. RESULTS AND DISCUSSION

A. Temporal evolution of aluminum ablation plume

Figure 4 shows a typical temporal sequence of soft-x-ray absorbance images of an aluminum ablation plume from 0 to 30 ns after femtosecond laser irradiation with an intensity of 4.2×10^{14} W/cm^2. We particularly investigated the 71 to 86 eV energy region, which corresponds to the region near the $L_{II,III}$ absorption edge of solid aluminum, because the absorption spectrum near the edge can be expected to reflect the variety of aluminum particles produced by the ablation process. The image sequence clearly shows that the aluminum plume expanded from the aluminum tape surface toward a vacuum as the time delay increased. Here we note certain characteristics that we observed in these images in time delay order.

At a time delay of 0 ns, we observed very weak absorption of the plume near the tape surface. This is probably due to the absorption of the plume that expanded during the initial 30 ps of laser irradiation. The absorption of the plume then gradually increased and certain characteristic structures clearly appeared in the absorbance image as the time delay increased from 500 ps to 5 ns. First, two line structures be-

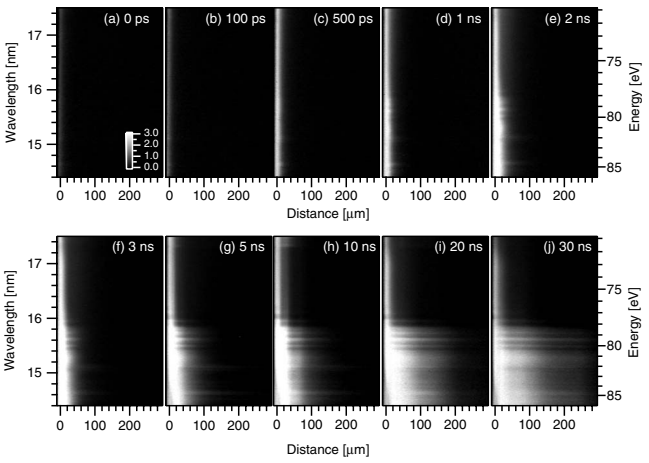

FIG. 4. Temporal sequence from 0 to 30 ns of spectrally resolved soft-x-ray absorbance images in the 71–86 eV energy region of an aluminum plume that was induced by a laser irradiation with an intensity of 4.2×10^{14} W/cm^2. Each image shows the absorbance spectrum of the aluminum plume as a function of the distance from the aluminum tape surface that corresponds to the distance of 0 μm. An absorbance image, μ_d, is defined as $\mu_d=\ln(I_0/I)$, where I_0 and I are the reference image without the plume absorption and the transmission spectrum with the plume absorption, respectively. Each image consists of 3000 shots.

came noticeable in the 81–85 eV energy region from 500 ps and they spread more quickly toward the vacuum. Then, three absorption lines and an absorption band appeared in the 78–82 eV energy region from 1 ns. Lastly, an edge structure with a width of about 1 eV could be recognized near 72 eV from 2 ns. In the long time delay from 10 to 30 ns, the characteristic structures in the absorbance image remained almost unchanged except for the significant expansion of the plume. Thus, the improvement of the spectral resolution revealed that the absorbance images of the plume are composed of these spectral structures, which we could not resolve in our previous study.[26,30]

Figure 5 shows the temporal variation in the amount of ejected plume generated at an irradiation laser intensity of 4.2×10^{14} W/cm^2. We roughly estimated the variation in the

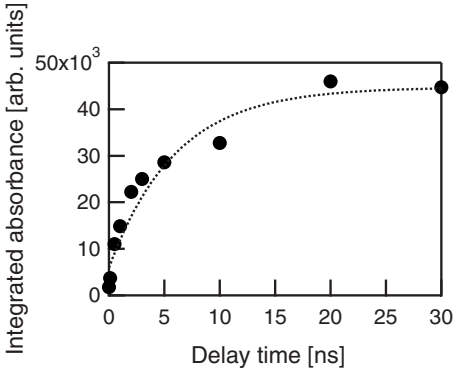

FIG. 5. Temporal variation in spatially and spectrally integrated absorbance of the aluminum plume that was generated at a laser irradiation intensity of 4.2×10^{14} W/cm^2. Dashed curve is a guide to the eyes.

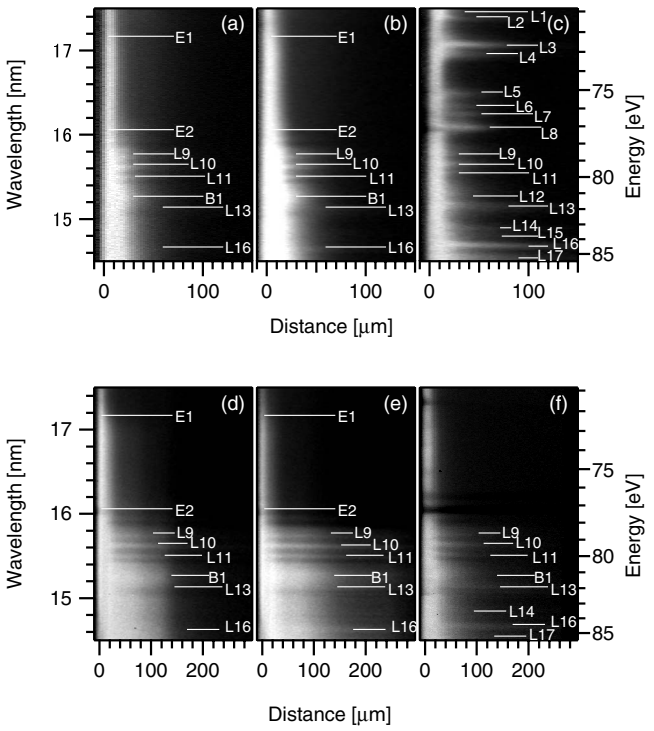

FIG. 6. Laser irradiation intensity dependence of the absorbance image of the aluminum plume at delay times of [(a)–(c)] 3 ns and [(d)–(f)] 30 ns. The irradiation intensity corresponds to [(a) and (d)] 1.8×10^{14} W/cm^2, [(b) and (e)] 4.2×10^{14} W/cm^2, and [(c) and (f)] 8.5×10^{14} W/cm^2, respectively. The labels in the figure are the same ones used in Fig. 7 and Table I.

amount by integrating the plume absorbance spatially and spectrally. This figure shows that the total absorbance of the plume increased steeply in the early stages (from 0 to 5 ns) and then it saturated 10–30 ns after the laser irradiation. The saturation of the plume absorption indicates that the plume ejection from the surface had almost finished by this time, namely, it takes a few tens of nanoseconds for the plume to be ejected from the irradiated surface.

B. Intensity dependence of absorbance image

We also investigated the dependence of the plume absorbance image on the laser irradiation intensity from 1.8×10^{14} to 8.5×10^{14} W/cm^2. For absorbance images at a time delay of 3 ns, the absorbance spectra structures change significantly according to the laser irradiation intensity. The absorbance image at a low irradiation intensity of 1.8×10^{14} W/cm^2 showed characteristic absorption edge structures near 72 and 77 eV and absorption lines near 80 eV [Fig. 6(a)]. At a medium irradiation intensity of 4.2×10^{14} W/cm^2, the absorption lines near 82 and 85 eV, which are shown in Fig. 4, appeared in addition to these structures [Fig. 6(b)]. When the irradiation intensity was 8.5×10^{14} W/cm^2, the absorbance image clearly changed compared to these images and was dominantly composed of many intense absorption lines [Fig. 6(c)]. This observation suggests that the dominant particle generated through the

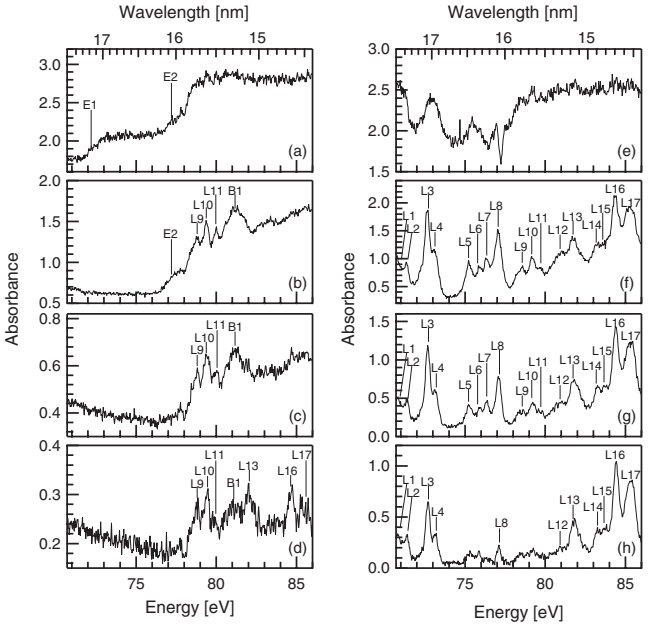

FIG. 7. Typical profiles at various distances from the tape surface selected from absorbance images obtained at a time delay of 3 ns and laser irradiation intensities of [(a)–(d)] 1.8×10^{14} W/cm^2 and [(e)–(h)] 8.5×10^{14} W/cm^2. Each profile was obtained by averaging the absorbance images in the [(a) and (e)] 0–11 μm, [(b) and (f)] 22–33 μm, [(c) and (g)] 44–55 μm, and [(d) and (h)] 66–77 μm regions. The assignments of all the spectral structures labeled in the figure are summarized in Table I.

ablation process depends strongly on the laser irradiation intensity.

For the absorbance images at a time delay of 30 ns, the edge structure near 72 eV exhibited a clear spatial dependence as the plume expanded at a low irradiation intensity [Fig. 6(d)]. In contrast to the absorbance spectrum at the medium irradiation intensity [Fig. 6(e)], an edge structure near 77 eV was clearly observed in this absorbance spectrum. At a high irradiation intensity, the absorption lines disappeared, particularly those in the 71–77 eV energy region, while many intense absorption lines were observed in this region at 3 ns [Fig. 6(f)]. In addition, there are dip structures near 71.5 and 77 eV in Fig. 6(f). They are probably due to intense line emissions from oxygen ions and aluminum ions, respectively. Since these line emissions from the plume itself cause a diplike structure in an absorbance spectrum, it should be noted that the dip structure does not originate in the absorbance spectrum of the plume.

C. Identification of ablation particles in aluminum plume

The improvement in the spectral resolution enables us to discuss the identification of each ablation particle based on an analysis of the spectral structures observed in the absorbance images. For the analysis, we selected two typical absorbance images obtained at laser irradiation intensities of 1.8×10^{14} and 8.5×10^{14} W/cm^2 and at a time delay of 3 ns [Figs. 6(a) and 6(c)]. Figure 7 shows their profiles at various distances from the tape surface. All the spectral structures labeled in Fig. 7 and their assignments are summarized in Table I. Moreover, we successfully estimated the spatial distribution of the average atomic density of each ablation particle at various time delays as a result of the assignment (Fig. 8).

At a laser irradiation intensity of 1.8×10^{14} W/cm^2, the two edge structures labeled as E1 and E2 can be clearly observed in the near surface region [Figs. 7(a) and 7(b)]. In our recent letter, we showed that the component characterized by the E1 edge corresponds to nanometer-sized aluminum particles in the liquid phase by combining three pieces of experimental evidence.[31] Briefly, the first is that the energy position and the broadening of the E1 edge can be explained by the L edge of the liquid aluminum phase at high temperature.[35,36] The second piece of evidence is the large difference between the densities of the liquid component and normal liquid phases. The typical atomic density of about 3×10^{19} atoms/cm^3 [Fig. 8(a)], which corresponds to 1.5×10^{-3} g/cm^3, is much lower than the density of normal liquid aluminum (2.3 g/cm^3).[37] This low density of the liquid component strongly suggests that it corresponds to liquid particles with a local density that remains high but with the average density becoming low. The last piece of evidence is that the absorption of the liquid component decreased with the irradiation intensity [Figs. 6(d)–6(f)]. This is very similar to the laser intensity dependence of the nanometer-sized particle generation via femtosecond laser ablation.[25] In contrast to our identification of the liquid nanoparticles, Glover and co-workers[38,39] reported that silicon particles exhibited a solid-liquid-solid phase transition within 50 ps of laser irradiation by using time-resolved core-level photoemission spectroscopy (TR-CPS). Their conclusion was based on the observation that the peak of silicon $2p$ ($L_{\mathrm{II,III}}$) electron binding energy shifted 1.3 eV lower immediately after the laser irradiation and then rapidly returned to the original energy level of solid silicon. However, several experimental studies reported that the binding energy of the silicon $2p$ electrons shifted to a higher energy of the order of 2 eV owing to the transformation from semiconductor to metal electronic state when laser melting occurred.[40–42] Therefore, there is room for reconsideration in their experimental interpretation that the ultrafast solidification of nanoparticles occurs via femtosecond laser ablation. As we pointed out, one possible reason for this experimental discrepancy is the difference of probing region between XAS and core-level photoemission spectroscopy (CPS).[30] Although this discrepancy still cannot be completely explained, our observations strongly suggest that the nanoparticles travel in a vacuum as a hot liquid phase.[31]

The E2 edge is different from the L_{I} edge of solid aluminum because the L_{I} edge is positioned at about 118 eV.[34] The E2 edge can be clearly observed while the E1 edge almost disappears in the 22–33 μm region in Fig. 7(b). This indicates that the E2 edge corresponds to one independent component of the plume. Although the identification of the E2 edge structure is currently unclear, one possibility is that the component characterized by the E2 edge corresponds to an aluminum atomic cluster. The energy of the E2 edge is about 77 eV, which is between the energy of the $L_{\mathrm{II,III}}$ edge of solid aluminum and that of the neutral atom.[43] It is reasonable to assume that an aluminum atomic cluster has its $L_{\mathrm{II,III}}$ edge

TABLE I. Assignments of the spectral structures of the aluminum ablation particles labeled in Fig. 7.

Label	E_{obs} [a] (eV)	I_{obs}	Assignment	E_{calc} (eV)	Ref.	Notes[b]
E1	72.2		Liquid Al, $L_{II,III}$ edge		35	
E2	77.2		Unknown			Atomic cluster
B1	81.2		Unknown			Al
L1	70.8	1.05	Al^+, $2p^63s3p$-$2p^53s^23p$	70.81	47	
L2	71.3	0.94	Al^+, $2p^63s3p$-$2p^53s^23p$	71.22	47	
L3	72.7	1.87	Al^{2+}, $2p^63s$-$2p^53s^2$	72.91	45	
L4	73.0	1.17	Al^{2+}, $2p^63s$-$2p^53s^2$	73.33	45	
L5	75.2	0.97	Unknown			Al
L6	75.9	0.85	Unknown			Al
L7	76.4	0.99	Unknown			Al
L8	77.0	1.53	Unknown			Al
L9	78.6	0.87	Al, $2p^63s^23p$-$2p^53s^23p4s$	78.78	44	
L10	79.2	1.04	Al, $2p^63s^23p$-$2p^53s^23p4s$	79.38	44	
L11	79.7	0.83	Al, $2p^63s^23p$-$2p^53s^23p4s$	79.78	44	
L12	81.0	1.14	Al^+, $2p^63s^2$-$2p^53s3p^2$	81.28	44	
L13	81.7	1.33	Al^+, $2p^63s^2$-$2p^53s3p^2$	81.63	45	
L14	83.3	1.26	Al^+, $2p^63s^2$-$2p^53s^24s$	83.12	45	
L15	83.6	1.24	Al^+, $2p^63s^2$-$2p^53s^24s$	83.51	45	
L16	84.4	2.10	Al^+, $2p^63s^2$-$2p^53s^23d$	84.56	45	
L17	85.3	1.91	Al^+, $2p^63s^2$-$2p^53s^23d$	85.25	45	

[a]Energy values of labels E, B, and L are obtained from Figs. 7(a), 7(b), and 7(f), respectively.
[b]Tentative assignment based on the data shown in Fig. 7. See the discussion in the text.

between these two values.[27] However, further investigation will be necessary for a clear identification of the E2 edge.

At a higher laser irradiation intensity of 8.5×10^{14} W/cm^2, we observed a large number of line structures over the entire region [Figs. 7(e)–7(h)]. As shown in Table I, most of the absorption lines labeled in Fig. 7(f) can be identified unambiguously as resonance transitions of aluminum neutral atoms, singly charged ions, and doubly charged ions based on previously obtained data.[44–47] In the near surface region, the line structures are not well resolved as a result of the broadening of each absorption line [Fig. 7(e)], but the spectral structures in this region roughly correspond to that in the 22–33 μm region [Fig. 7(f)]. The broadening of the absorption lines is probably due to the high-temperature and high-density effect on each ablation particle in the near surface region. In Figs. 7(b)–7(d), an absorption band (labeled B1) is clearly observed near 81 eV. Since this band generally appears with the three absorption lines of neutral atoms, it may be assigned as neutral atoms. One possibility is that it corresponds to the L edge of the neutral atoms.[43] In addition, we discuss unidentified absorption lines, which are labeled from L5 to L8, in Fig. 7(f). It should be noted that these four absorption lines and the neutral atom absorption lines gradually decrease as the distance from the tape surface decreases [Figs. 7(f)–7(h)] and they are hardly observed at a low irradiation intensity [Figs. 7(b)–7(d)]. These experimental results indicate that the four absorption lines correspond to the transitions of neutral atoms in the excited state and not in the ground state. We also estimated the spatial distribution of the average atomic density of neutral atoms and singly charged ions in the ground state at various time delays by using the absorption lines labeled L10 and L16 [Figs. 8(b) and 8(c)]. In the region extending from the tape surface to 250 μm, the average atomic density of both neutral atoms and singly charged ions ranged from about 1×10^{19} to 2×10^{17} atoms/cm^3.

At this laser irradiation intensity, we found that the absorption lines in the 71–77 eV energy region (L1–L8) almost disappeared while those in the 77–86 eV region (L9–L17) remained at a time delay of 30 ns [Fig. 6(f)]. This intensity reduction of the absorption lines was observed from a time delay of 20 ns. The absorption lines that disappeared correspond to doubly charged ions in the ground state, singly charged ions in the excited state, and probably neutral atoms in the excited state, while the remaining absorption lines correspond to the ground states of neutral atoms and singly charged ions. Therefore, this observation indicates that ablation particles in a higher energy state are unstable compared to those in the ground state and their lifetimes range from 20 to 30 ns.

D. Ablation dynamics in the early stages of plume expansion

The clear identification of ablation particles in the plume enables us to discuss the ablation dynamics in the early stages of the plume expansion based on experimental observation. We show the temporal evolution of particle ejection from the tape surface at an irradiation intensity of 4.2

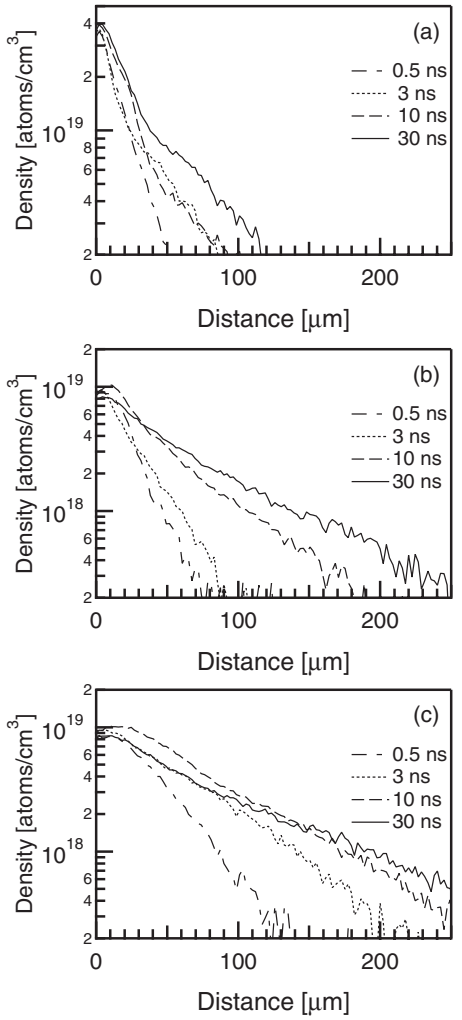

FIG. 8. Spatial distribution of the average atomic density of (a) the liquid nanoparticles generated at an irradiation intensity of 1.8×10^{14} W/cm^2, (b) neutral atoms generated at an irradiation intensity of 8.5×10^{14} W/cm^2, and (c) singly charged ions generated at an irradiation intensity of 8.5×10^{14} W/cm^2. Each curve corresponds to the data at a time delay of 0.5 ns (broken), 3 ns (dotted), 10 ns (dash-dotted), and 30 ns (solid), respectively. To estimate the atomic density, we assumed that the length of the plume transmitted by the soft-x-ray beam corresponded to the beam diameter of the laser pulse used for ablation generation. For the liquid nanoparticles, we assumed a mass absorption coefficient of aluminum at 74 eV, which was obtained from the absorbance spectrum of solid aluminum shown in Fig. 3. For singly charged ions, we used the mass absorption coefficient of the most intense line labeled by L16 (Ref. 45). For neutral atoms, we used the same mass absorption coefficient used for singly charged ions for the absorption line labeled L10 because there are no data for the absorption coefficient of neutral atoms.

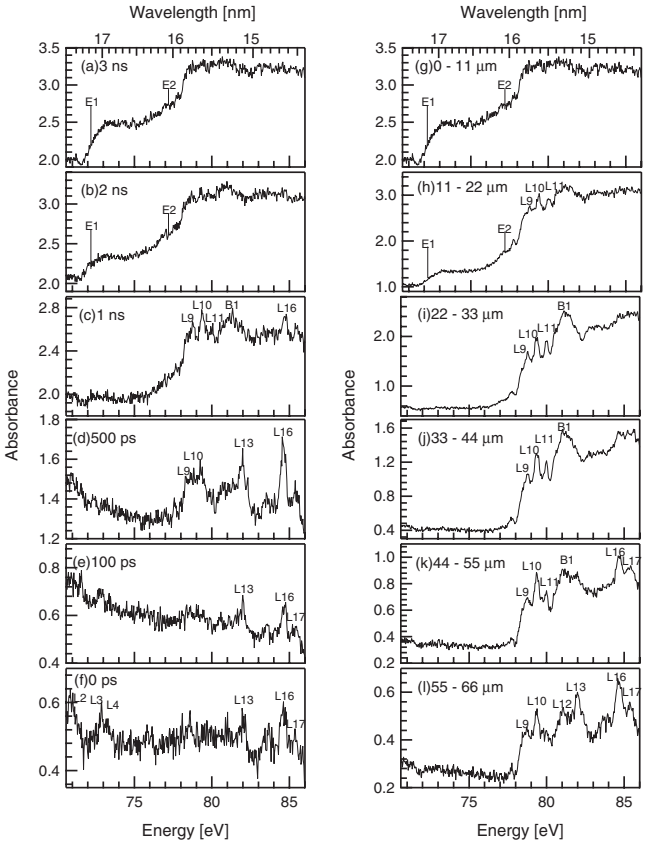

FIG. 9. [(a)–(f)] Temporal evolution of particle ejection from the tape surface at time delays from 0 ps to 3 ns and [(g)–(l)] the spatial distribution of each particle obtained at a time delay of 3 ns obtained at an irradiation intensity of 4.2×10^{14} W/cm^2.

$\times10^{14}$ W/cm^2 in Figs. 9(a)–9(f). Each profile was obtained by averaging the absorbance image in the near surface region of 0–11 μm. The figures clearly show that each ablation particle is ejected sequentially from the surface region. First, the intense absorption lines near 82 and 84.5 eV of singly charged ions clearly appeared at 0 ps. In addition, the absorption lines of singly charged ions in the excited state and doubly charged ions in the ground state may appear near 71 eV. In the subsequent time delays of 100 and 500 ps, singly charged ions in the ground state were still dominant while singly charged ions in the excited state and doubly charged ions were scarcely detectable. Then, neutral atoms, which are characterized by the three absorption lines near 79 eV and the absorption band at 81 eV, appeared at 1 ns while the singly charged ions largely disappeared. After the appearance of the neutral atoms, liquid nanoparticles and, probably, atomic clusters appeared at 2 and 3 ns. The two components subsequently remained dominant in the near surface region until 30 ns. To compare these observations to the temporal evolution of the particle ejection, we show the spatial distribution of each particle obtained at a time delay of 3 ns and the same irradiation intensity [Figs. 9(g)–9(l)]. The figures clearly show that the singly charged ions, neutral atoms, liquid nanoparticles, and atomic clusters are distributed according to their distance from the tape surface. A comparison of these figures clearly shows that the early ejected components, namely, the singly charged ions, reach a region distant from the tape surface, while the late ejected components, namely, the liquid nanoparticles and atomic clusters, remain largely near the tape surface. This suggests that the plume consists of ablation particles with different ejection velocities.

We estimated the average expansion velocities up to 3 ns of singly charged ions, neutral atoms, and liquid nanopar-

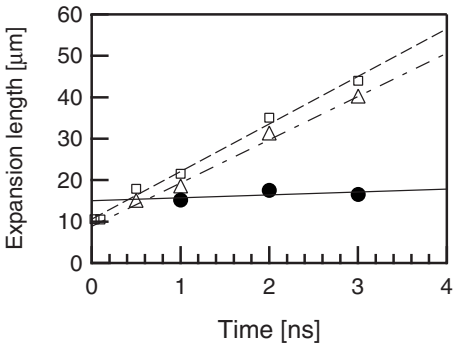

FIG. 10. Transient expansion length obtained at an irradiation intensity of 4.2×10^{14} W/cm^2 as a function of time delay of singly charged ions (open squares), neutral atoms (open triangles), and liquid nanoparticles (filled circles) up to 3 ns. Each average ejection velocity is estimated from data line fitting (solid line).

ticles by obtaining their transient expansion lengths as a function of time delay (Fig. 10). Fitting the density distributions at 84.5, 79.4, and 74 eV with an exponential function enables us to obtain the transient expansion lengths of singly charged ions, neutral atoms, and liquid nanoparticles, respectively. This figure suggests that the plume separates into gaseous particles with a high velocity of about 1.1×10^4 m/s and nanoparticles with a slow velocity of about 6.9×10^2 m/s. Of the gaseous particles, singly charged ions are slightly faster than neutral atoms. In a previous investigation with time-gated optical emission spectroscopy, the ejection velocities of the gaseous particles and nanoparticles in an aluminum ablation plume were approximated from a plot of emission intensity versus time delay.[6] The velocities of the gaseous particles and the nanoparticles agree well with the average velocity reported in the study (1.2×10^4 m/s for the gaseous particles and 1.0×10^3 m/s for the nanoparticles). The good coincidence of the nanoparticle velocity strongly supports the view that the liquid aluminum component observed in our study corresponds to nanometer-sized aluminum particles.

E. Physical mechanism of short-pulse ablation well above ablation threshold

We use our observations for a qualitative discussion of the physical mechanism of femtosecond laser ablation for irradiation intensity well above the ablation threshold. At an irradiation intensity of 4.2×10^{14} W/cm^2, which is well above the ablation threshold of aluminum (about $4-5\times10^{12}$ W/cm^2 for a 100 fs pulse[20,48]), we observed liquid nanoparticles, neutral atoms, and singly charged ions in the plume. For the production of ions or plasma from metals, the dynamics of ionization or plasma transition of aluminum induced by a 90 fs pulse with an intensity of 10^{13} W/cm^2 was investigated with a femtosecond time-resolved reflectivity measurement.[49] The observation of a significant reflectivity decrease within the pulse-width-limited fall time in this measurement indicates that the ionization roughly completes within the laser-pulse duration. Considering such ultrafast ionization, the production of singly charged ions observed in our study is likely to be induced by a mechanism related to optical-field ionization, which is generally accepted as an ultrafast ionization mechanism in ultrashort laser-pulse–gas interactions.[50] In fact, it is known that electrons within an optical skin depth are emitted from a metal surface by the photoelectric effect that is similar to multiphoton and tunneling ionization of atoms when the laser intensity is lower than ablation threshold.[51,52] When the laser intensity is high, the ejection of an enormous quantity of electrons from the metal surface may induce an initial ionization or plasma transition of the surface region on a time scale comparable to the laser-pulse duration.[53] This initial plasma state with near solid density is generally assumed in ultrashort laser-solid interactions.[50] Although the temporal resolution was insufficient for the time scale of this initial ionization in our study, the appearance of singly charged ions near the moment of the laser-pulse irradiation [Fig. 9(f)] qualitatively supports this idea of the ultrafast ionization mechanism. In addition, the observation that ion production was enhanced more significantly than that of the other two types of ablation particles at higher irradiation intensities [Fig. 6(c)] also supports the ionization mechanism that should strongly depend on a peak intensity of the laser pulse.

For the production of neutral atoms and liquid nanoparticles, their production mechanism at an irradiation intensity close to the ablation threshold has been investigated experimentally with time-resolved optical microscopy for various metals and semiconductors.[20–22] It was observed that characteristic transient interference fringes were typically sustained up to 5 ns at an irradiation intensity of 9.2×10^{12} W/cm^2.[20] The authors proposed that the fringes were formed as a result of interference between light reflected from the front and rear of the ablating layer, which is composed of a transparent inhomogeneous phase of gas and liquid particles with a high refractive index. It is currently accepted that the inhomogeneous phase of gas and liquid is produced through a process known as phase explosion or homogeneous boiling, where the initially molten homogeneous fluid generated immediately after femtosecond laser irradiation decomposes into a mixture of gas and liquid when it enters the liquid-vapor metastable region of the phase diagram. In contrast to their observation, our measurement strongly suggests that the gaseous particles of singly charged ions and neutral atoms start to separate from the liquid nanoparticles at 1 ns and are completely separate after at least 2 ns (Fig. 9). In the spatial distribution of the absorbance image, the liquid nanoparticles occupying the near surface region are clearly separate from the gaseous phase even at a time delay of 3 ns. This was supported by the large difference between the ejection velocities of the liquid particles and the gaseous phase. These observations indicate that the ablation mechanism observed in our study is different from phase explosion. The hypothesis is supported by the observation that the transient fringes only appear in a certain range of irradiation intensity above the ablation threshold.[54,55] When we consider that the laser irradiation intensity is well above the ablation threshold in our study, the most probable mechanisms explaining our experimental results are photomechanical fragmentation for nanoparticle production and vaporization for neutral atom production. Both were proposed and identified in recent

molecular-dynamics studies as important mechanisms for short-pulse ablation, especially in the energy region well above the ablation threshold.[10–14] Photomechanical fragmentation is a process whereby an initially molten homogeneous fluid decomposes into a collection of clusters as a result of the conversion of the stress induced by laser irradiation into strain during the subsequent thermal expansion.[10–14] Vaporization is the complete atomization that occurs when the laser energy is greater than the cohesive energy.[10,11] Since these two mechanisms can produce neutral atoms and liquid nanoparticles without the coexistence state of gas and liquid phases induced by the phase explosion process, our experimental results also support the proposition that photomechanical fragmentation and vaporization are responsible for the production of nanoparticles and neutral atoms, respectively, in femtosecond laser ablation that occurs well above the ablation threshold.

IV. CONCLUSION

In conclusion, we studied the dynamics of the expanding femtosecond laser ablation plume of aluminum generated in the 10^{14}–10^{15} W/cm^2 intensity range with a time-resolved one-dimensional XAFS imaging system that uses the combination of a femtosecond-laser-pump and picosecond-soft-x-ray-probe arrangement and a KB-type soft-x-ray microscope. We successfully assigned the ejected particles based on the spectral structures near the L absorption edge of the aluminum plume and clarified that the plume consists of doubly and singly charged ions, neutral atoms, liquid nanoparticles, and possibly atomic clusters. The spatiotemporal evolution of the ablation particles allowed us to estimate the spatial distribution of the atomic density and the ejection velocity of each type of particle. In particular, we focused on the temporal sequence of the particle ejection in the early stages of plume expansion within 3 ns of the irradiation. The results strongly supported the view that photomechanical fragmentation and vaporization are dominant mechanisms for the production of liquid nanoparticles and neutral atoms, respectively, in femtosecond laser ablation that occurs well above the ablation threshold. The possible mechanism of the production of ions was also discussed based on the results. Our study demonstrated that the time-resolved XAFS imaging technique is a valuable approach for investigating ultrafast spatiotemporal dynamics such as short-pulse laser ablation.

ACKNOWLEDGMENT

This work was partly financed by the Ministry of Education, Culture, Sports, Science and Technology of Japan under Grant-in-Aid for Scientific Research No. 16032219.

*oguri@nttbrl.jp

†Present address: Department of Chemistry, School of Science, the University of Tokyo, 7-3-1 Hongo, Bunkyo-ku, Tokyo 113-0033, Japan.

[1] F. Korte, J. Serbin, J. Koch, A. Egbert, C. Fallnich, A. Ostendorf, and B. N. Chichkov, Appl. Phys. A: Mater. Sci. Process. **77**, 229 (2003).

[2] Y. Shimotsuma, P. G. Kazansky, J. Qiu, and K. Hirao, Phys. Rev. Lett. **91**, 247405 (2003).

[3] F. Qian, R. K. Singh, S. K. Dutta, and P. P. Pronko, Appl. Phys. Lett. **67**, 3120 (1995).

[4] M. Okoshi, S. Higuchi, and M. Hanabusa, J. Appl. Phys. **86**, 1768 (1999).

[5] J. Perrière, E. Millon, W. Seiler, C. Boulmer-Leborgne, V. Craciun, O. Albert, J. C. Loulergue, and J. Etchepare, J. Appl. Phys. **91**, 690 (2002).

[6] S. Amoruso, R. Bruzzese, N. Spinelli, R. Velotta, M. Vitiello, X. Wang, G. Ausanio, V. Iannotti, and L. Lanotte, Appl. Phys. Lett. **84**, 4502 (2004).

[7] A. Vogel, J. Noack, G. Hüttman, and G. Paltauf, Appl. Phys. B: Lasers Opt. **81**, 1015 (2005).

[8] L. V. Zhigilei and B. J. Garrison, J. Appl. Phys. **88**, 1281 (2000).

[9] F. Vidal, T. W. Johnston, S. Laville, O. Barthélemy, M. Chaker, B. Le Drogoff, J. Margot, and M. Sabsabi, Phys. Rev. Lett. **86**, 2573 (2001).

[10] D. Perez and L. J. Lewis, Phys. Rev. Lett. **89**, 255504 (2002).

[11] D. Perez and L. J. Lewis, Phys. Rev. B **67**, 184102 (2003).

[12] D. Perez and L. J. Lewis, Appl. Phys. A: Mater. Sci. Process. **79**, 987 (2004).

[13] P. Lorazo, L. J. Lewis, and M. Meunier, Phys. Rev. Lett. **91**, 225502 (2003).

[14] P. Lorazo, L. J. Lewis, and M. Meunier, Phys. Rev. B **73**, 134108 (2006).

[15] C. Cheng and X. Xu, Phys. Rev. B **72**, 165415 (2005).

[16] S. Amoruso, R. Bruzzese, M. Vitiello, N. N. Nedialkov, and P. A. Atanasov, J. Appl. Phys. **98**, 044907 (2005).

[17] B. N. Chichkov, C. Momma, S. Nolte, F. von Alvensleben, and A. Tünnermann, Appl. Phys. A: Mater. Sci. Process. **63**, 109 (1996).

[18] C. Momma, S. Nolte, B. N. Chichkov, F. von Alvensleben, A. Tünnermann, H. Welling, and B. Wellegehausen, Opt. Commun. **129**, 134 (1996).

[19] C. Momma, B. N. Chichkov, S. Nolte, F. von Alvensleben, and A. Tünnermann, Appl. Surf. Sci. **109-110**, 15 (1997).

[20] D. von der Linde, K. Sokolowski-Tinten, and J. Bialkowski, Appl. Surf. Sci. **109-110**, 1 (1997).

[21] K. Sokolowski-Tinten, J. Bialkowski, A. Cavalleri, D. von der Linde, A. Oparin, J. Meyer-ter-Vehn, and S. I. Anisimov, Phys. Rev. Lett. **81**, 224 (1998).

[22] D. Von der Linde and K. Sokolowski-Tinten, Appl. Surf. Sci. **154-155**, 1 (2000).

[23] A. Miotello and R. Kelly, Appl. Phys. Lett. **67**, 3535 (1995).

[24] L. N. Dinh, S. E. Hayes, A. E. Wynne, M. A. Wall, C. K. Saw, B. C. Stuart, M. Balooch, A. K. Paravastu, and J. A. Reimer, J. Mater. Sci. **37**, 3953 (2002).

[25] S. Eliezer, N. Eliaz, E. Grossman, D. Fisher, I. Gouzman, Z. Henis, S. Pecker, Y. Horovitz, M. Fraenkel, S. Maman, and Y. Lereah, Phys. Rev. B **69**, 144119 (2004).

[26] Y. Okano, K. Oguri, T. Nishikawa, and H. Nakano, Rev. Sci. Instrum. **77**, 046105 (2006).
[27] H. van Brug, K. Murakami, F. Bijkerk, and M. J. van der Wiel, J. Appl. Phys. **60**, 3438 (1986).
[28] T. Ohyanagi, A. Miyashita, K. Murakami, and O. Yoda, Jpn. J. Appl. Phys., Part 2 **33**, 2586 (1994).
[29] P. Kirkpatrick and A. V. Baez, J. Opt. Soc. Am. **38**, 766 (1948).
[30] Y. Okano, K. Oguri, T. Nishikawa, and H. Nakano, Appl. Phys. Lett. **89**, 221502 (2006).
[31] K. Oguri, Y. Okano, T. Nishikawa, and H. Nakano, Phys. Rev. Lett. **99**, 165003 (2007).
[32] D. Kühlke, U. Herpers, and D. von der Linde, Appl. Phys. Lett. **50**, 1785 (1987).
[33] H. Nakano, T. Nishikawa, H. Ahn, and N. Uesugi, Appl. Phys. Lett. **69**, 2992 (1996).
[34] C. Gähwiller and F. C. Brown, Phys. Rev. B **2**, 1918 (1970).
[35] J. A. Catterall and J. Trotter, Philos. Mag. **8**, 897 (1963).
[36] C. F. Hague, Phys. Rev. B **25**, 3529 (1982).
[37] M. J. Assael, K. Kakosimos, R. M. Banish, J. Brillo, I. Egry, R. Brooks, P. N. Quested, K. C. Mills, A. Nagashima, Y. Sato, and W. A. Wakeham, J. Phys. Chem. Ref. Data **35**, 285 (2006).
[38] T. E. Glover, G. D. Ackerman, A. Belkacem, P. A. Heimann, Z. Hussain, R. W. Lee, H. A. Padmore, C. Ray, R. W. Schoenlein, W. F. Steele, and D. A. Young, Phys. Rev. Lett. **90**, 236102 (2003).
[39] T. E. Glover, G. D. Ackerman, R. W. Lee, and D. A. Young, Appl. Phys. B: Lasers Opt. **78**, 995 (2004).
[40] K. Murakami, H. C. Gerritsen, H. van Brug, F. Bijkerk, F. W. Saris, and M. J. van der Wiel, Phys. Rev. Lett. **56**, 655 (1986).
[41] S. L. Johnson, P. A. Heimann, A. M. Lindenberg, H. O. Jeschke, M. E. Garcia, Z. Chang, R. W. Lee, J. J. Rehr, and R. W. Falcone, Phys. Rev. Lett. **91**, 157403 (2003).
[42] K. Oguri, Y. Okano, T. Nishikawa, and H. Nakano, Appl. Phys. Lett. **87**, 011503 (2005).
[43] P. Indelicato, S. Boucard, and E. Lindroth, Eur. Phys. J. D **3**, 29 (1998).
[44] A. M. Cantù, G. P. Tozzi, and N. Spector, J. Opt. Soc. Am. **72**, 729 (1982).
[45] J. B. West, T. Andersen, R. L. Brooks, F. Folkmann, H. Kjeldsen, and H. Knudsen, Phys. Rev. A **63**, 052719 (2001).
[46] J. T. Costello, D. Evans, R. B. Hopkins, E. T. Kennedy, L. Kiernan, M. W. D. Mansfield, J.-P. Mosnier, M. H. Sayyad, and B. F. Sonntag, J. Phys. B **25**, 5055 (1992).
[47] J. P. Mosnier, J. T. Costello, E. T. Kennedy, L. Kiernan, and M. H. Sayyad, Phys. Rev. A **49**, 755 (1994).
[48] M. Kandyla, T. Shih, and E. Mazur, Phys. Rev. B **75**, 214107 (2007).
[49] X. Y. Wang and M. C. Downer, Opt. Lett. **17**, 1450 (1992).
[50] P. Gibbon and E. Förster, Plasma Phys. Controlled Fusion **38**, 769 (1996).
[51] C. Tóth, G. Farkas, and K. L. Vodopyanov, Appl. Phys. B **B53**, 221 (1991).
[52] C. Lemell, X.-M. Tong, F. Krausz, and J. Burgdörfer, Phys. Rev. Lett. **90**, 076403 (2003).
[53] M. M. Murnane, H. C. Kapteyn, S. P. Gordon, and R. W. Falcone, Appl. Phys. B: Lasers Opt. **58**, 261 (1994).
[54] A. Cavalleri, K. Sokolowski-Tinten, J. Bialkowski, M. Schreiner, and D. von der Linde, J. Appl. Phys. **85**, 3301 (1999).
[55] B. Rethfeld, V. V. Temnov, K. Sokolowski-Tinten, S. I. Anisimov, and D. von der Linde, Proc. SPIE **4760**, 72 (2002).